Spin-triplet supercurrents of odd and even parity in nanostructured devices

Lahabi, K.

Citation

Lahabi, K. (2018, December 4). *Spin-triplet supercurrents of odd and even parity in nanostructured devices*. *Casimir PhD Series*. Retrieved from https://hdl.handle.net/1887/68031

Author: Lahabi, K.
Title: Spin-triplet supercurrents of odd and even parity in nanostructured devices
Issue Date: 2018-12-04

7

SPONTANEOUS EMERGENCE OF JOSEPHSON JUNCTIONS IN SINGLE-CRYSTAL Sr_2RuO_4

Yuuki Yasui[†], Kaveh Lahabi[†], Victor Fernández Becerra, Muhammad Shahbaz Anwar, Shingo Yonezawa, Takahito Terashima, Milorad V. Milošević, Jan Aarts & Yoshiteru Maeno

---

This work is to be submitted for publication.

[†] These authors contributed equally to this work.

Author contributions: The crystals were grown in the group of Y. Maeno at Kyoto University. K. Lahabi FIB-structured the crystals that were prepared by Y. Yasui. Y. Yasui performed the transport measurements. M. S. Anwar took part in the discussion. S. Yonezawa and Y. Maeno supervised the measurements. K. Lahabi and Y. Yasui analysed the results. K. Lahabi formulated the discussion presented in Section 7.4. Y. Yasui modelled the Little-Parks oscillations. V. F. Becerra and M. V. Milošević (University of Antwerp) carried out the TDGL simulations; and aided with the theoretical input. K. Lahabi and Y. Yasui wrote the paper with inputs from all the authors.

7.1. GENERAL INTRODUCTION

THE OXIDE Sr_2RuO_4 stands out among the unconventional superconductors as one of the very few materials with spin-triplet pairing and broken time-reversal symmetry [1, 2]. The tetragonal crystal structure allows five unitary representations for a p-wave pairing symmetry [1, 3]. One of these is the chiral order parameter, of the form $p_x \pm i p_y$, which is strongly suggested by muon spin relaxation [4] and high-resolution polar Kerr effect measurements [5] (see Section 2.2.3).This equal-spin pairing state is attracting renewed attention due to the possibility that it can host Majorana bound states, which in turn are of interest for topological quantum computing [6–8]. A key property of the chiral state is its double degeneracy in the orbital degree of freedom, with important consequences such as the emergence of domains of different chirality and the existence of an edge current.

The major hurdle plaguing our understanding of Sr_2RuO_4 is that, although the chiral state seems probable, domains or edges currents have not been observed directly [9]. Indications for their existence however have been found in transport experiments, which utilize Ru inclusions to form proximity junctions between Sr_2RuO_4 and a conventional s-wave superconductor (see Figure 7.1**a-c**). These systems exhibit highly unconventional transport properties, which have been attributed to the presence of chiral domains [10, 11]. Typical examples of this are presented in Figure 7.1. A complication in the physics of Sr_2RuO_4 is that, by lifting the tetragonal crystal symmetry, the Ru inclusions, or uniaxial strain in general, can induce a different superconducting state [12, 13] with an enhanced $T_c \approx 3$ K. Recent studies suggest that this "extrinsic" phase (also known as the 3 K-phase) may have an even-parity order parameter, and is most likely non-chiral (i.e. single-component)[1] [14, 15]. The exact pairing symmetry of this state is yet to be determined, however, this means that transport experiments have so far been conducted on hybrids of S-Ru-Sr_2RuO_4(extrinsic)-Sr_2RuO_4(intrinsic)-Sr_2RuO_4(extrinsic)-Ru-S. While such hybrids are fascinating on their own merits, their capacity to directly inform us on the unspoiled chiral phase is limited.

More importantly, the vast majority of studies of the past two decades have been limited to bulk Sr_2RuO_4 crystals, typically hundreds of microns in dimension. This is mainly due to the absence of thin superconducting Sr_2RuO_4 films. The domains, however, are expected to be no more than a few microns in size, and to have an arbitrary arrangement (presumably pinned by random defects in the lattice) [16, 17]. Moreover, the time-dependent "telegraph noise" which is in observed in transport measurements suggests the domains are mobile [10, 11].

---

[1] In this chapter we refer to the superconducting phase at 1.5 K, which corresponds to the multi-component (i.e. chiral) order parameter proposed for pure Sr_2RuO_4 as intrinsic, and the possible single-component phase, characterized by a broad transition at $T \approx 3$ K (strain-induced), as extrinsic.

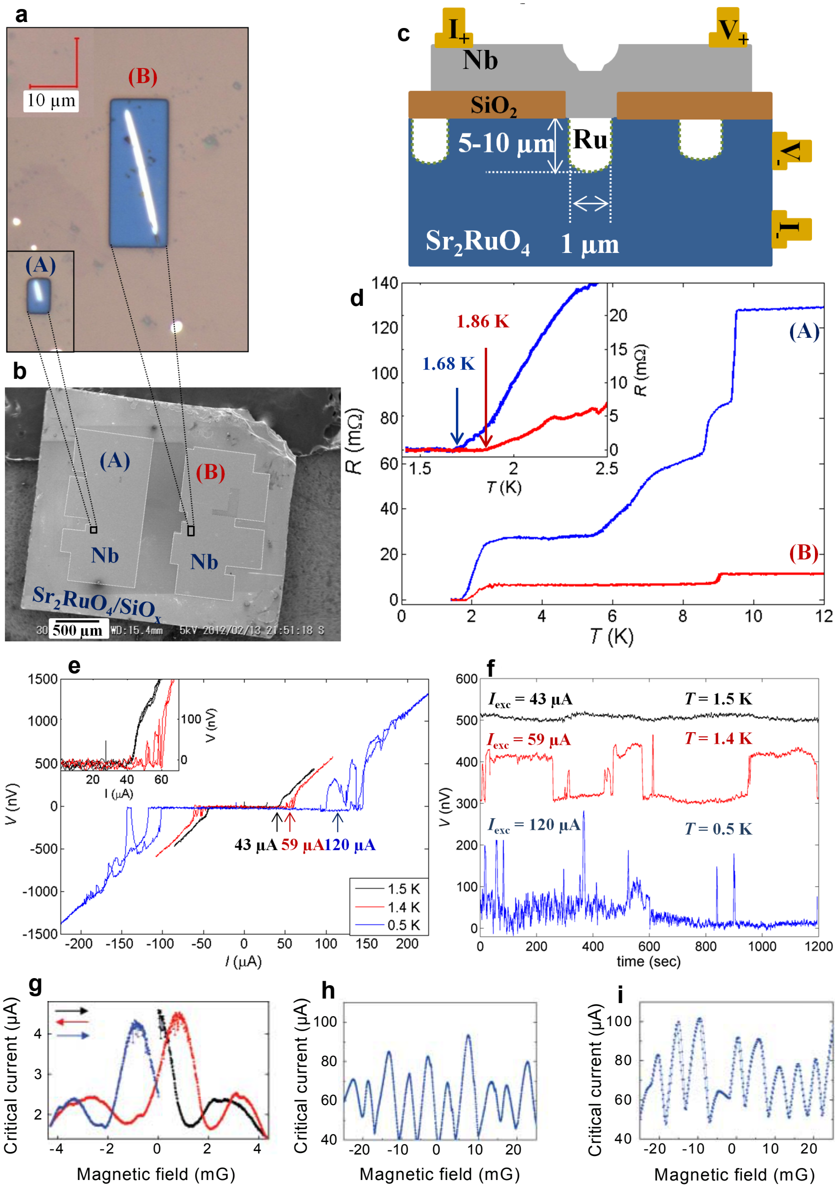

Figure 7.1: Examples from previous transport experiments. **a** Ru inclusions, used for making electrical contact with Sr_2RuO_4. **b** a typical Sr_2RuO_4 crystal used in transport experiments. The dimensions are of the order of a few millimeters. **c** schematic of a Sr_2RuO_4 proximity junction. **d** multistage $R(T)$ transitions, typical for Sr_2RuO_4 proximity junctions. The characteristic feature of these systems is the broad transition observed around 2.5-3 K, corresponding to the extrinsic phase that forms around Ru inclusions. **e,f** switching of voltage. The “telegraphic noise” appears under a d.c. current bias, and has been attributed to current-excited chiral domain wall (ChDW) motion (**a-f** reproduced from Ref. [10]). **g** example of a hysteretic interference pattern, suggesting field-induced ChDW motion. **h-i** change of interference pattern in the same device at different thermal cycles, suggesting the reconfiguration of ChDWs (**g-i** reproduced from Ref. [11]).

The stochastic arrangement of the domains, combined with the unavoidable presence of an extrinsic phase (around the Ru contacts), introduce an inherent uncertainty in the analysis of such experiments. This also means that theoretical calculations cannot predict a unique outcome for a given transport measurement. We avoid these restrictions by implementing a new approach to directly probe nanostructured Sr_2RuO_4 crystals with a homogenous phase, that can be either extrinsic or intrinsic. This enables us to examine each phase separately (in different samples), and compare their behaviour. We show that the use of high-quality nanostructures, combined with time-dependent Ginzburg-Landau (TDGL) simulations, provides a powerful tool for the study chiral of superconductivity in a controllable manner, where theoretical predictions can be directly verified by transport experiments.

7.2. INTRODUCTION

Mesoscopic structures of a chiral p-wave superconductor are expected to host multichiral states [18], where the two $p_x \pm ip_y$ chiral components of the order parameter segregate into domains, separated by a chiral domain wall (ChDW). On the other hand, the energy cost associated with a ChDW grows per area [17]. This makes mesoscopic structures a promising platform to verify, and potentially control the domains. Another remarkable aspect of a ChDW is that it can act as a Josephson junction [17] by locally suppressing the condensate between the two chiral states, as shown in Figure 7.2. What makes this particularly significant is that, depending on its orientation relative to the transport direction, a ChDW junction could have a nontrivial Josephson phase ϕ, where $0 < \phi < \pi$ [17].

Here we present the results of transport measurements on mesoscopic rings of Sr_2RuO_4, prepared by focused ion beam (FIB) milling of single crystals. Homogeneous structures with an intrinsic phase, characterized by a sharp transition at 1.5 K, show a distinct critical current oscillation—similar to that of the classical dc superconducting quantum interference device (SQUID), with two artificially prepared Josephson junctions. Despite the absence of conventional weak links, the oscillations persist over a surprisingly wide temperature range (well below T_c) while maintaining their overall shape. Interestingly, this behavior is entirely absent in structures that are in the extrinsic phase. These systems behave as standard superconducting loops: they exhibit conventional T_c oscillations (i.e. Little-Parks) which can only be observed near the transition [19]. We also present data from calculations of possible chiral configurations in the ground state of a p-wave superconducting ring, using the Ginzburg-Landau formalism. Experiments and calculations together make a convincing case for two chiral domain walls being present in the two arms of the ring, leading to the observed SQUID-like behavior.

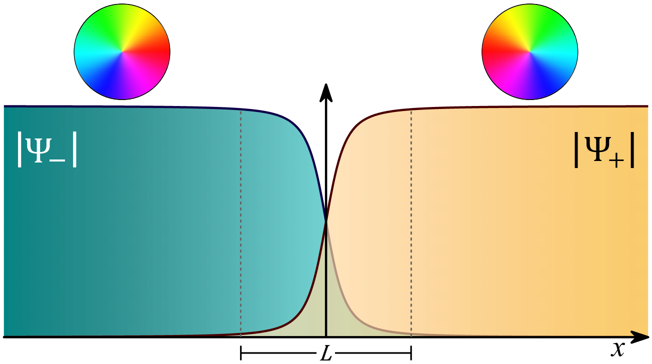

Figure 7.2: **Schematic of a chiral domain wall.** Ψ_- and Ψ_+ correspond to the chiral states $p_x - ip_y$ and $p_x + ip_y$, which meet at the ChDW. A Josephson junction is formed as the two chiral components overlap over a finite distance $L \propto \xi$, and induce a local suppression of the superconducting condensate. The colour wheels represent the orbital phase of each chiral component.

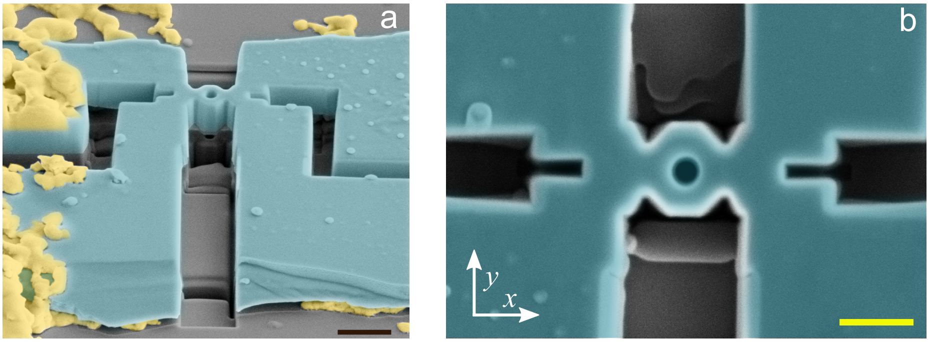

Figure 7.3: **Falsed-color scanning electron microscope image of the ring yy146. a** blue and yellow, respectively, represent the Sr_2RuO_4 crystal and the silver epoxy used for making electrical contact. The ring is connected to four transport leads, and is sculpted out of a 0.7 μm thick crystal by a Ga^+ focused ion beam. The surface of the crystal is protected by a 100 nm SiO_x layer. **b**, close-up of the ring. The outer radius is 1.1 μm, and the inner radius is at least 0.2 μm. The dark and yellow scale bars correspond to 2 μ m and 1 μ m, respectively.

7.3. RESULTS

7.3.1. BASIC TRANSPORT PROPERTIES

Single crystals of Sr_2RuO_4 were grown with the floating zone method [20] and structured into microrings using Ga-based FIB etching. Figure 7.3 show scanning electron microscope (SEM) images of such a ring (called yy146), with an inner radius r_{in} of 200 nm (minimum), an outer radius r_{out} of 550 nm, and a thickness of 700 nm.

The temperature-dependent resistance $R(T)$ of this ring, presented in Figure 7.4 **a**, shows a rather sharp superconducting transition.The high quality of the sample is

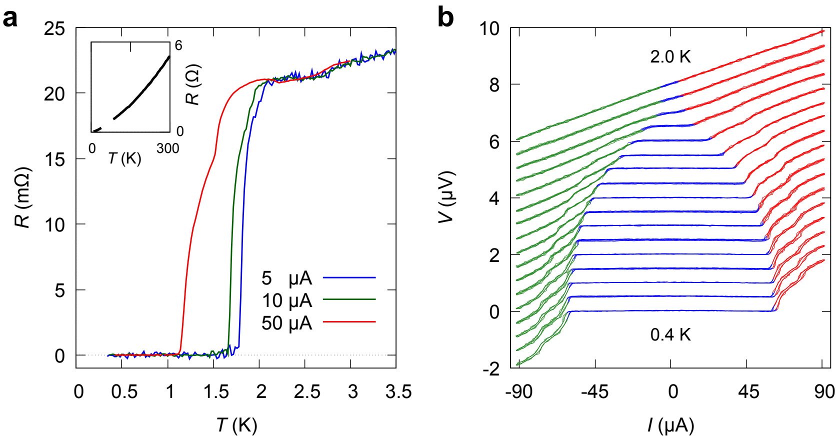

Figure 7.4: Basic transport properties of sample yy146. **a** resistance as a function of temperature R(T) measured with different d.c. currents. The insets show R(T) in a wider temperature range. The ratio of residual resistivity (RRR) is 238. **b** current-voltage ($I-V$) characteristics for the temperature range between 2 K and 0.4 K, measured in steps of 0.1 K. The colours green, blue and red correspond to voltages $V < -0.1\ \mu$V, $-0.1\ \mu\text{V} < V < 0.1\ \mu$V and $0.1\ \mu\text{V} < V$, respectively. The curves are offset from each other for clarity. At each temperature, the curve consists of multiple $I-V$ traces, measured while sweeping the d.c. bias in both directions as $0 \rightarrow I^+ \rightarrow I^- \rightarrow I^+$ in repeated scans.

evident by its particularly high residual resistivity ratio (RRR = 238). Comparing Figure 7.4 **a** with the $R(T)$ measured before structuring the crystal, we find that the ring maintains the same superconducting transition as the initial crystal (see Supplementary Figure 7.S1). We find no discernible changes in the overall transport properties of the material, as might have been introduced by microstructuring the crystal. A set of current-voltage ($I-V$) characteristics, taken at different temperatures, is shown in Figure 7.4 **b**. The critical current I_c develops around 1.7 K, and begins to saturate below 0.8 K. We find the hysteresis in $I-V$ around I_c to remain negligibly small, even at temperatures far below T_c.

7.3.2. INSIGHTS FROM ORDER PARAMETER SIMULATIONS

Before presenting the results of transport measurements in a magnetic field, we examine the expected chiral-domain configuration in our structure. This is accomplished by performing detailed time-dependent Ginzburg-Landau simulations, under the assumption of a chiral p-wave order parameter, for microrings with nanostructured transport leads (similar to the one used in our experiments). The simulations show that the ring can host single- or a multi-chiral domain states, depending on the parameters r_{in}/ξ and r_{out}/ξ, which correspond to the inner and outer radius of the ring, scaled by the (temperature-dependent) coherence length ξ.

In Figure 7.5 we present the key aspects of the simulations related to our particular structure. However, the complete phase diagram of various ground states was also

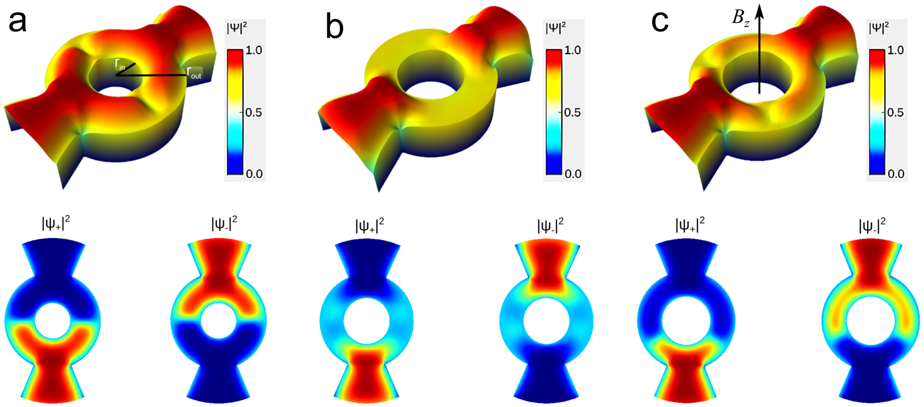

Figure 7.5: Ground state configurations of a chiral p-wave ring with nanostructured transport leads. The colourmap represents the Cooper pair density. The bottom panels shows the Cooper pair density for each chiral component separately. **a,b** simulated ground states in the absence of external fields, at temperatures $T \ll T_c$ and $T \approx T_c$, respectively. **a** corresponds to a state where the two chiral components are segregated by a single domain wall, while for **b** the chiral components are overlapping with each other, and are equally suppressed. **c** shows the behaviour of the chiral domain state in **a** under an applied out-of-plane magnetic field. In all three states the ring hosts a multi-domain configuration, where the suppression of the condensate results in the formation of a pair of parallel weak links, similar to a DC SQUID.

calculated as a function $(r_{\text{in}}/\xi, r_{\text{out}}/\xi)$. Figure 7.5**a** shows the simulated ground state of our ring for $T \ll T_c$, obtained by setting $r_{\text{in}}/\xi \approx 2.2$ and $r_{\text{out}}/\xi \approx 6.1$, while setting $\xi(T = 0) \approx 66$ nm. This shows two distinct chiral domains, separated by a single ChDW in each arm of the ring. The ChDW extends over a length of the order of ξ. Within this region, the order parameter is reduced to about half of its amplitude in the banks, resulting in the formation of two parallel Josephson weak links.

The chiral states in the other temperature limit, where for $T \sim T_c$ is presented in Figure 7.5 **b**. This corresponds to a state where $\xi(T) \sim w$, where $w = r_{\text{out}} - r_{\text{in}}$. We see that the order parameter is suppressed over a significantly larger portion of the arms. While this may appear as an extended ChDW, it corresponds to a different state, which should be described as one of overlapping chiral domains. Intuitively, one can picture this as a mixed state, where the two chiral components are both present and equally suppressed over the entire ring. As they overlap with each other, their amplitudes are reduced to about a third of the original value in the transport leads. However, from the physics point of view, the suppression of $|\Psi|$ still produces a pair of stable weak links.

Figure 7.5 **c** shows the $T \ll T_c$ state in presence of a finite magnetic field applied along the ring axis $(\Phi = 2.4\Phi_0)$. Pinned by the restricted dimensions, the ChDWs remain in the arms of the ring, though their positions are shifted away from the middle. This is because, depending on its direction, the applied field enlarges one chiral domain over the other. Nevertheless, the simulations show that a multi-domain state with parallel weak links, formed by ChDWs, is stable in our ring while performing field-dependent measurements, to which we now turn.

7.3.3. CRITICAL CURRENT OSCILLATIONS

We examined the supercurrent interference properties of the ring by applying an out-of-plane magnetic field H_z. Figure 7.6 presents the I_c measured for positive I_c^+ and negative I_c^+ currents, at two different temperatures — representing $T \sim T_\mathrm{c}$ and $T \ll T_\mathrm{c}$ regimes. For both temperatures we observe distinct critical current oscillations, with the period corresponding to fluxoid quantization over the ring area. This distinct pattern strongly resembles that of the classical dc SQUID with two artificially prepared weak links. Figure 7.6 also shows $-I_\mathrm{c}^-(-H)$ overlaid on its time-reversed counterpart $+I_\mathrm{c}^+(+H)$ for comparison.

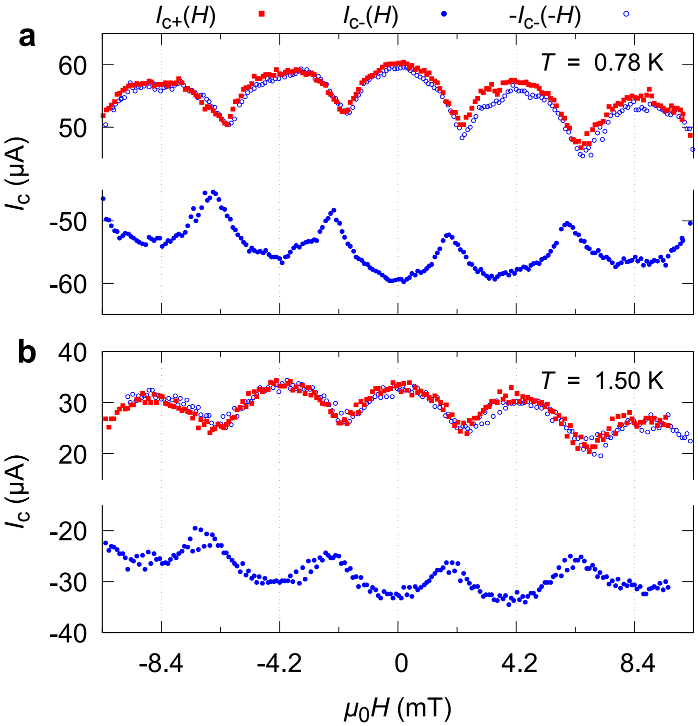

Figure 7.6: Critical current as a function of magnetic field for positive (I_c^+) and negative (I_c^-) d.c. bias measured at 0.78 K ($T = 0.45\ T_\mathrm{c}$) **(a)**, and 1.5 K ($T = 0.85\ T_\mathrm{c}$) **(b)**. $-I_\mathrm{c}^-(-H)$ represents the time-reversed counterpart of $I_\mathrm{c}^+(+H)$.

To demonstrate the robustness of the SQUID behaviour, in Figure 7.6 we plot the magnetoresistance signal, produced by the I_c oscillations over a wide range of temperatures. These are measured by applying a constant d.c bias while sweeping the field. As the magnitude of $I_c(H_z)$ oscillates between $I_c < I$ and $I_c > I$, the system is driven out and back into the zero-voltage regime of the $I-V$ curve. This produces nonlinear variations in voltage, which we measure for $+I$ and $-I$ biases. We represent this as resistance, using the definition $R = [V(I) - V(-I)]/2I$.

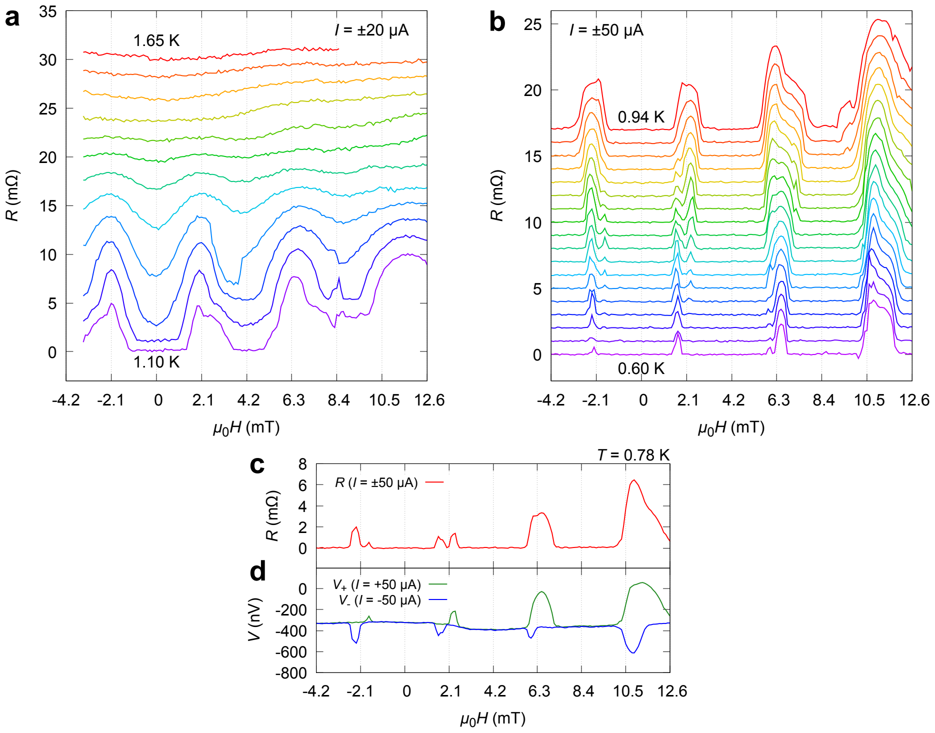

Figure 7.7: Magnetotransport over a wide range of temperatures. Non-linear variations in voltage, driven by (SQUID) I_c oscillations, result in a periodic large-amplitude magnetoresistance signal $R(H)$ (**a,b**) which appears with the onset of the transition, and continues to be present at temperatures far below T_c. The temperature steps are ≈ 50 mK, and the $R(H)$ traces are offset from each other for clarity. **c,d** show how the magnetovoltage from $I_\pm$ is converted to $R(H)$.

Figure 7.7**a,b** show the results collected over a broad range of temperatures. These reveal that the SQUID oscillations emerge together with I_c at the onset of the transition, and continue to be present for all $T < T_c$. In Figure 7.7**c** we account for the shape of $R(H)$, where in some cases the peaks can appear to be split or broadened. This is due to a slight difference in the values of $I_c^\pm$, which causes the peaks in $V(\pm I)$ to appear asymmetrically.

The magnetovoltage signal and field-dependent $I-V$ measurements are crucial for resolving an issue regarding previous reports of unconventional behaviour of Sr_2RuO_4 rings. Cai *et al.* have consistently observed magnetoresistance oscillations with unexpectedly large amplitude [21, 22]. Their reported magnetoresistance oscillations are also stable over a wide range of temperatures, reaching far below T_c (see Figure 3a in Ref. [21]). As Figure 7.7 demonstrates however, if the magnetovoltage signal is divided by a constant dc bias, it produces the same type of magnetoresistance as the ones reported by Cai *et al.* . Hence, what appears as large-amplitude magnetoresistance is in fact the nonlinear variation of voltage, driven by an oscillating critical current.

7.3.4. RINGS WITH AN EXTRINSIC PHASE & T_c OSCILLATIONS

To verify that the observed behaviour is an inherent property of the intrinsic phase of Sr_2RuO_4, and a multicomponent order parameter, we examined a number of structures with a full or partial extrinsic phase. These are characterised by a noticeably broader transition, which begins near 3 K (see Figure 7.8**a**). We recently reported observations of Little-Parks (LP) oscillations in such structures [19], and here we show that those are of a completely different character than the I_c oscillations found in the a pure (bulk-like) intrinsic phase.

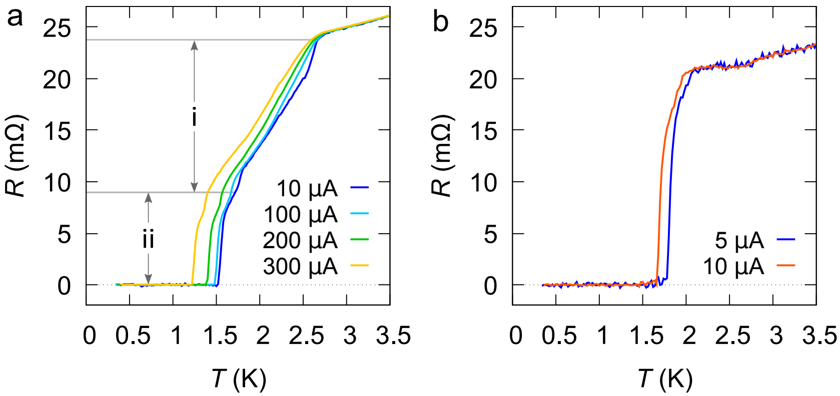

Figure 7.8: Comparing resistance transitions for the extrinsic & intrinsic phases of Sr_2RuO_4. **a** resistance transitions in sample yy150. The $R(T)$ curve is divided into two separate regimes. **i** corresponds to the superconducting transition in the loop itself, and also indicates the region where the Little-Parks oscillations are observed. **ii** shows the transition in the transport leads. The leads have a sharp transition around 1.5 K, which is associated with the intrinsic phase of Sr_2RuO_4. The ring itself however, exhibits a broad transition with an onset at 2.6 K. This is a clear characteristic of the extrinsic phase, which appears under uniaxial strain (e.g. see 7.1 **d**). **b** $R(T)$ measurements from sample yy146, shown here for comparison. The bulk-like transition corresponds to a structure with a homogenous intrinsic phase.

In particular, we compare the above data (taken from sample yy146) with those of a second ring called yy150. This ring was also fabricated from a bulk crystal with a T_c of 1.5 K. After structuring however, the ring was found to have an enhanced T_c, where the transition already starts at 2.6 K. As indicated in Figure 7.8**a**, the ring itself is predominantly in the extrinsic phase, which was most likely introduced by the fabrication process (probably due to a strain induced by FIB milling). Compared

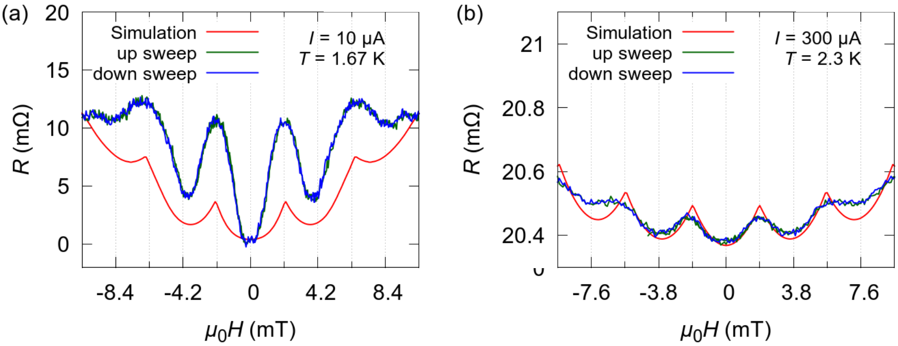

Figure 7.9: Simulated magnetoresistance for T_c oscillations. **(a)** sample yy146. The measurements signal is dominated by a large-amplitude magnetovoltage, driven by the (SQUID) I_c oscillations. **(b)** sample yy150. The absence of SQUID oscillations in a system with a dominant extrinsic phase allows us to observe the small-amplitude magnetoresistance signal produced by the Φ_0-periodic oscillations in T_c. The loop exhibits standard behaviour, and the oscillations can be modelled by the conventional Little-Parks effect.

to yy146 (RRR= 238), this ring has a smaller ratio of residual resistance RRR = 129. Nevertheless, the high RRR value still indicates strong and homogeneous metallicity.

In Figure 7.9, we show the $R(H_z)$ measurements for both rings, taken at temperatures within the resistive transition. In both rings we find fluxoid-periodic oscillations, which we compare with those simulated for the LP effect. This serves as a reference for the standard behaviour of a homogenous superconducting loop. The LP effect refers to the Φ_0-periodic suppression of T_c, which appears as a small magnetoresistance oscillation for measurements taken at the resistive transition of a superconducting loop [23]. The change of the transition temperature due to the LP oscillations is given by [24]:

$$\frac{T_c(B_z)-T_c(0)}{T_c(0)} = \left(\frac{\pi\xi(0)\,wB_z}{\sqrt{3}\Phi_0}\right)^2 - \frac{\xi^2(0)}{r_{in}r_{out}}\left(n-\frac{\pi r_{in}r_{out}B_z\pi}{\Phi_0}\right)^2 \qquad (7.1)$$

where $\xi(0)$ is the coherence length at 0 K, n is an integer, r_{in} and r_{out} are the inner and outer radii of the ring, and $w = r_{out} - r_{in}$ is the width. The first term of Equation 7.1 represents the effect of the Meissner shielding, and the second term represents the effect of the fluxoid quantization. To convert the change of the transition temperature to the resistance variation, we assume that the $R(T)$ curve does not change its shape under magnetic field and shifts horizontally by$\Delta T_c = T_c(0) - T_c(B_z)$. The simulations in Figure 7.9 were obtained using $\xi(0) = 66$ nm as the coherence length of Sr_2RuO_4, and $2r_{in} = 0.55\ \mu$m, $2r_{out} = 1.1\ \mu$m for sample yy146, and $2r_{in} = 0.7\ \mu$m, $2r_{out} = 1\ \mu$m for yy150.

For sample yy150, both the period and the amplitude of the oscillations agree with those of the simulation. It is therefore clear that the oscillations are the result of standard the LP effect, and are driven by T_c oscillations. In contrast, for sample yy146, the amplitude of the observed $R(H)$ oscillations is substantially larger than what T_c variations can produce. This is because the oscillations in yy146 are driven by $I_c(H)$. As shown in Figure 7.7, the I_c oscillations produce *non-linear* variations in voltage, which heavily dominate the signal resulting from T_c oscillations. Note that the LP oscillations correspond to a *linear* $I-V$ relation, whose slope gently attenuates by fluxoid quantization, resulting in a small variation of (ohmic) resistance.

The contrast in the behavior of the two systems can be demonstrated more directly by comparing their $I-V$ characteristics at low temperatures. These are presented in Figure 7.10 in the form of $I-V$ traces, and their first derivatives. Unlike sample yy146, the critical current oscillations are completely absent in yy150, the ring which showed standard LP oscillations. We found this behavior to be common for all the systems with a dominant extrinsic phase that were measured (see Supplementary Figure 7.S2). While these systems vary in shape and dimensions, they consistently showed standard T_c variations, which could only appear in the $R(H)$ measured at $T \approx T_c$, but no sign of SQUID oscillations at any temperature.

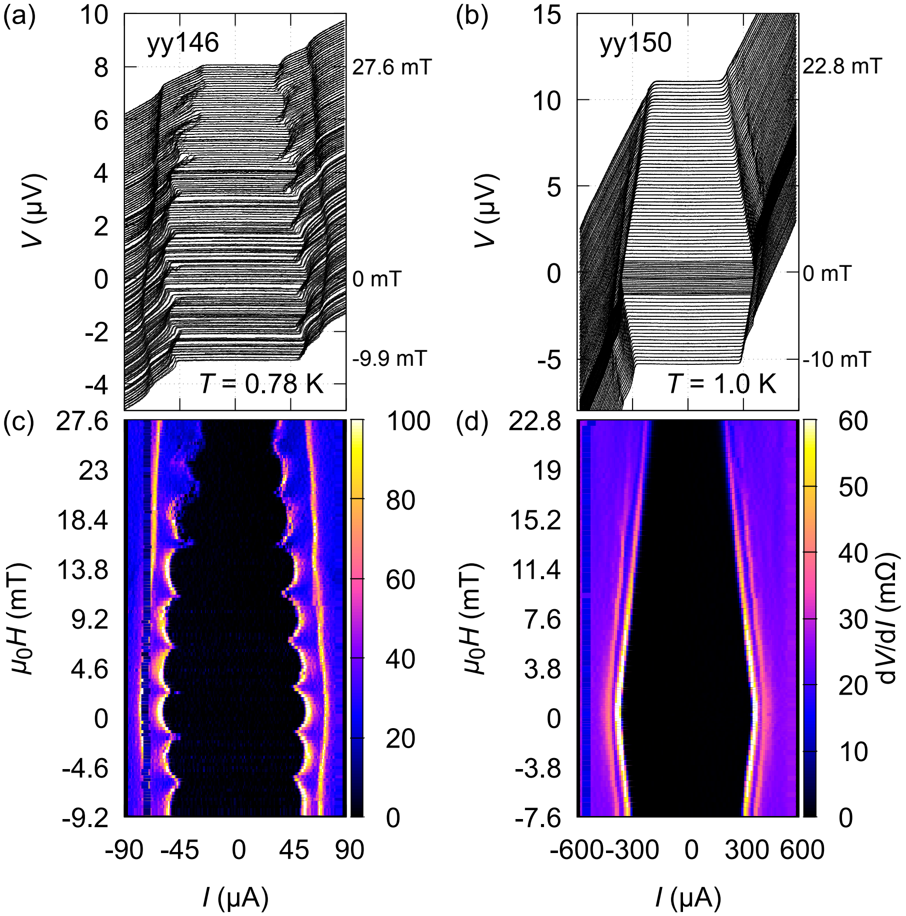

Figure 7.10: $I-V$ characteristics as a function of magnetic field: extrinsic vs. intrinsic phases. **a,b** $I-V$ traces measured while scanning $\mu_0 H_z$ in steps of 0.1 mT at $T \approx 0.45\ T_c$ for samples yy146 and yy150. **a** shows the SQUID oscillations of sample yy146, which represents the intrinsic phase of Sr_2RuO_4. **b** oscillations entirely absent in sample yy150, which has a predominantly extrinsic phase. **c,d** dV/dI plots obtained from the $I-V$ traces in **a,b**, demonstrating the contrast between the intrinsic and the extrinsic phase, corresponding to yy146 and yy150, respectively. **c** (**d**) shows the presence (absence) of the I_c oscillations in the intrinsic (extrinsic) phase found in yy146 (yy150).

7.3.5. ANOMALOUS CURRENT-VOLTAGE & IN-PLANE FIELDS

Figure 7.11**a** shows the anomalous $I-V$ characteristic of sample yy146, which occurs at 0.78 K for $\mu_0 H_z$ = 2 mT, where we observe a clear asymmetry with respect to the applied current bias. While voltage variations show standard behaviour for positive bias, the $I-V$ traces split into two separate paths depending on the sweep direction of negative bias. This results in an unusual hysteresis, where the $-I(V = 0) \rightarrow -I(V \neq 0)$ transition occurs at smaller currents than it does when sweeping I as $-I(V \neq 0) \rightarrow -I(V = 0)$, which is a clear contradiction to the standard $I-V$ hysteresis. This unusual $I-V$ characteristic appears to be of a similar nature as the ones reported for the so-called φ-junction, where the Josephson energy has a bistable zero-voltage state with phases $+\varphi$ and $-\varphi$, where $0 < \varphi < \pi$ [25, 26]. A similar scenario can occur at the ChDW, depending on the relative configuration of the domains [17]. This is described in Section 7.4.2.

The unconventional $I-V$ characteristics can be enhanced by applying rather small in-plane fields ($H_{ab} < 3\% H_{c1}$). Figure 7.12 shows sets of $I-V$ traces taken while scanning the out-of-plane field. Prior to each set of measurement, the sample was cooled through T_c under a constant in-plane field in the x-direction. While the period and amplitude of the original $I_c(H_z)$ pattern (responsible for the SQUID behavior) remains mostly intact, the in-plane field introduces a series of unusual non-zero voltage states which occur at $I < I_c$. Unlike the previous reports of unconventional $I-V$ characteristics in (s-wave) superconductor-Sr_2RuO_4 hybrids (e.g. see Figure 7.1 **e**), the observed voltage anomalies are highly robust and stable. For a given combi-

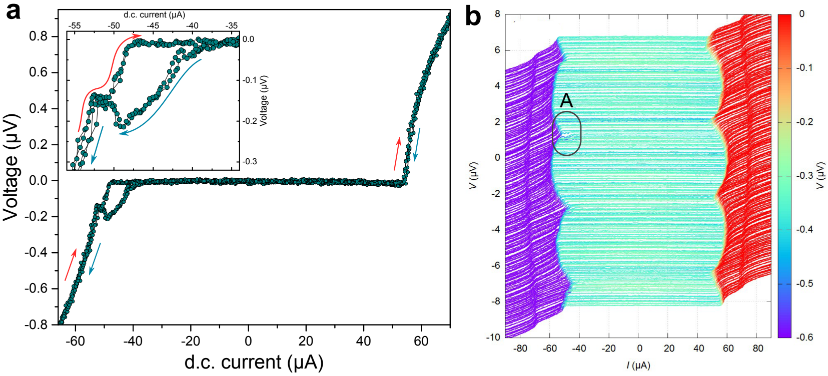

Figure 7.11: Anomalous $I-V$ characteristic in the absence of external in-plane fields. **a**, asymmetric step-like feature observed at $\mu_0 H_z = 2$ mT. Inset is the close up of the voltage transitions that occur at negative bias, with red and blue arrows indicating forward and reverse sweep directions of the applied current, respectively. The $I-V$ curve is measured by scanning I as $0 \rightarrow I^+ \rightarrow I^- \rightarrow I^+ \rightarrow I^-$ in two cycles. As shown here, the anomaly is highly stable and reproducible in repeated measurements. **b** shows individual $I-V$ curves taken over a wide range of out-of-plane fields, in steps of 0.1 mT. **A** indicates the region where the $I-V$ anomaly is observed.

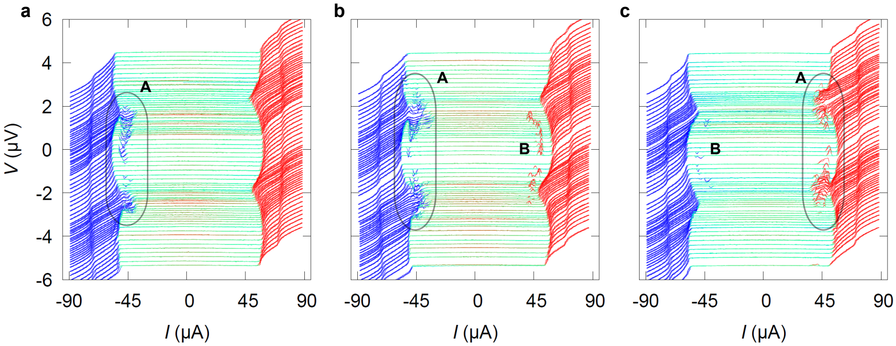

Figure 7.12: Anomalous $I-V$ characteristics & their relation with in-plane fields. Prior to each set of H_z scan, the sample is heated to its normal state and then cooled down to 0.78 K under a constant magnetic field, applied in x-direction. **a**, **b** and **c** correspond to field cooled measurements with $\mu_0 H_x = 0.5$ mT, 1 mT and -1 mT, respectively. The $I-V$ anomalies appear in two different forms, which are labelled as **A** and **B**. **A** appears at $I \approx I_c$, and is more pronounced near the minima of the interference pattern. **B** takes place on the opposite side of the $I-V$ curve, where there are no features near the $I_c(H_z)$ minima. These are isolated non-zero voltage peaks, which appear deep within the zero-voltage regime $I < I_c$. The anomalies show a direct relation with the sign and amplitude of H_x. As shown in **c**, switching the polarity of H_x reverses the order in which **A** and **B** appear.

nation of H_x and H_z, the same $I-V$ trace could be reproduced in multiple cooling cycles, with no discernable changes in the size or position of the voltage anomalies.

The anomalies also exhibit a direct relation with the sign and amplitude of the external in-plane field. For instance, at $\mu_0 H_x = 0, 0.5$ mT and 1 mT (Figures 7.11**b** & 7.12 **a,b**) the distortion of $I-V$ is highest near the I_c minima for $I < 0$ (labelled as **A**), while the anomalies remain minimal for I^+ (labelled as **B**). Remarkably, we find this asymmetric trend to be fully reversible by switching the sign of the in-plane field, as shown in Figure 7.11 for $\mu_0 H_x = -1$ mT.

The asymmetric interference patterns also indicate the breaking of time-reversal symmetry (TRS), as the condition $I_c^+(+H_z) = I_c^-(-H_z)$ is violated. We attribute this to the asymmetric orientation of the domains, which could induce an arbitrary phase difference across the ChDW. As for the role of in-plane fields, there are a number of possibilities related to spin polarization. These are discussed in Section 7.4.2.

7.4. DISCUSSION

7.4.1. MECHANISMS FOR OSCILLATORY $I_c(H)$

Before adopting ChDWs as the origin of the observed I_c oscillations, we consider other known mechanisms for such oscillations. In a homogenous loop, I_c can be modulated by the circulating persistent current I_p, which varies linearly with flux, and switches its direction every $\Phi_0/2$. This mostly results in a sawtooth-like modulation of I_c [27], which cannot account for the non-linear form of the patterns shown in Figure 7.6. Furthermore, the magnitude of I_p is inversely proportional to the kinetic inductance L_k, which depends on the penetration depth $L_k \propto \lambda^2(T)$. If the oscillations were driven by circulating currents, the amplitude of ΔI_c would grow larger by lowering the temperature, since $\Delta I_c \propto I_p \propto 1/\lambda^2(T)$ [27]. In contrast, Figure 7.6 shows that $\Delta I_c \approx 12\mu$A for both temperatures.

As we noted above, the large magnetoresistance found by Cai *et al.* in their Sr_2RuO_4 rings is also a form of I_c oscillation, which they attributed to current-excited vortices moving across the ring [21, 22]. Vortex motion can indeed result in magnetoresistance oscillations with considerably larger amplitude. However, as demonstrated by Berdiyorov *et al.* [28], the large-amplitude oscillations only occur over a finite temperature range. While increasing the measurement current could shift the oscillations to lower temperatures than Little-Parks, the range for large-amplitude oscillations remains relatively narrow, usually no more than 5% below T_c (e.g. see Figure 5b of Ref. [28] and Figure 2 of Ref. [29]). In contrast, the Sr_2RuO_4 rings with the intrinsic 1.5 K phase (including the ones reported by Cai *et al.*) consistently yield a large magnetoresistance signal for all $T < T_c$ (see Figure 7.7 and Figure 3a in Ref. [21]).

The observed I_c oscillations can be understood in terms of the quantum interference of macroscopic wavefunctions. With the exception of homogenous loops whose dimensions are smaller than $\xi(T)$ [30] (i.e. not applicable here since $r \lessapprox 4\xi(T)$ at $T =$ 0.78 K, such interference would require a pair of parallel Josephson junctions. These correspond to well-defined weak links where (at least) two macroscopic wavefunctions can overlap, and yield a *single-valued* current-phase relation (CPR). Weak links can be intrinsic to the material (e.g. cuprates, grain boundaries) or artificially prepared (e.g. bridges, proximity effect in SNS and SIS junctions). In either case, the suppression of the order parameter must be stable enough to produce a single-valued CPR [31]. We also note that the junctions responsible for the observed SQUID behaviour must be rather symmetric with respect to each other, since asymmetric I_c values could not produce the distinct cusp-shaped minima of the interference patterns in Figure 7.6.

Geometrical constrictions (e.g. bridges and nanowires) are known to serve as Josephson junctions, if their dimensions are comparable to ξ. It is well established that the

CPR of such Junctions is defined by the ratio of $\xi(T)$ to the length of the weak link, L. Since $\xi(T)$ varies with temperature, while L remains fixed, the CPR of such weak links is known to be strongly temperature dependent. Generally, lowering the temperature from T_c is known to transform a sinusoidal CPR into a sawtooth-like curve, which ultimately turns into multivalued relations for $L \gtrsim 3.5\xi(T)$ (corresponding to the nucleation of phase-slip centres) [31–33]. The multivalued CPR manifests itself as a hysteretic $I-V$ relation, which is a highly common characteristic of constriction junctions at $T \ll T_\mathrm{c}$ [34, 35]. This is in direct contrast to the $I-V$ measurements presented in Figure 7.4 **b**, which show negligible hysteresis for temperatures as low as 0.2 T_c, where $L \gtrsim \xi(T)$. Furthermore, the patterns taken at $T = 0.45\ T_\mathrm{c}$ and 0.85 T_c (Figure 7.6 **a** & **b**) have the same overall shape; which indicates that they most likely correspond to the same CPR. Whereas for constriction junctions, the oscillations would have been heavily deformed by the pronounced difference in $\xi(T)/L$. In case of ChDWs however, the size of the junction is determined by the coherence length (see Figure 7.2). This means that, instead of having a fixed value, L has a similar temperature dependence as $\xi(T)$. Therefore, compared to constriction junctions, the $\xi(T)/L$ ratio of a ChDW remains unaffected by lowering the temperature. This accounts for the lack of hysteresis in the $I-V$ (Figure 7.4 **b**), and the unperturbed shape of the interference patterns in Figure7.6.

In certain cases, phase-slip lines are also known to act as effective weak links. In a homogenous loop, fast moving kinematic vortices crossing the arms can dynamically form a pair of effective weak links, and operate as a SQUID. This mechanism however is highly temperature sensitive. As demonstrated in Refs. [36, 37], phase slippage can only yield a SQUID behaviour for a strictly narrow temperature range near T_c. Hence, it cannot account for the Sr_2RuO_4 rings, where the I_c oscillations remain unchanged for all$T < T_\mathrm{c}$.

Lastly, we exclude the possibility of forming accidental proximity junctions by Ru inclusions, or any other normal metal. Apart from their apparent absence in the SEM images obtained while structuring the crystal, inclusions would have induced an extrinsic 3K-phase, which is absent in our ring and the ones measured by Cai *et al.* [21, 22]. Furthermore, the relative suppression of the superconducting gap in a normal metal weak link would cause it to have a lower T_c than the superconducting electrodes. This should appear as (at least) two distinct transitions in $R(T)$ measurements: one for the electrodes; and one for the proximized material in the weak link, which clearly is not the case here — as shown in Figure 7.4 **a** and Refs. [21, 22]. Tunnel junctions, which in some cases can form by grain boundaries or nanocracks, are also not applicable here. This is evident by the strong metallicity of the rings, and the exceptionally high values of RRR (Figure 7.4 **a**), which could not be produced in the presence of insulating barriers.

7.4.2. JOSEPHSON ENERGY OF A CHIRAL DOMAIN WALL

In this section we use the model developed by Sigrist and Agterberg (1999) [17] to describe the Josephson energy of ChDW as function of its orientation. The energy profile hosts stable and metastable states, whose phases are determined by the orientation of ChDW, and can take on *any* values between 0 and π. We consider how these states would appear in a sequence of bias current sweeps, and compare the expected outcome with our own $I - V$ measurements.

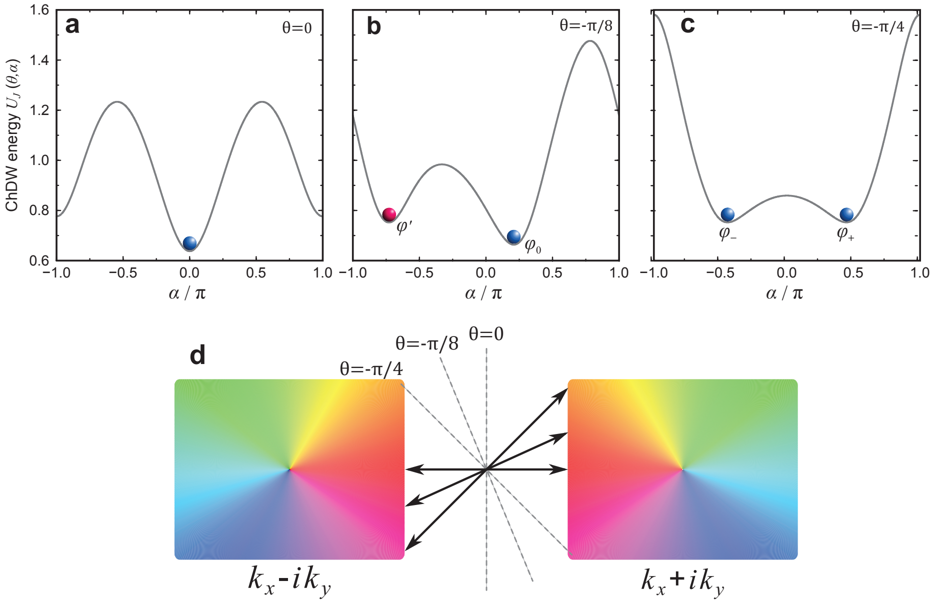

Figure 7.13: **Josephson energy of the chiral domain wall**. **a-c**, energy profiles of a chiral domain wall (ChDW) at various orientations relative to transport direction (θ). α is the phase difference between the two sides of the junction. **a**, $\theta = 0$, the junction has a stable phase at $\alpha = 0$ and a metastable phase at $\alpha = \pi$. **b**, $\theta = -\pi/8$. Compared to $\theta = 0$, the stable state (blue) has a higher energy, while the energy of the metastable state (red) is lowered. The junction has developed arbitrary phases φ_0 (stable) and φ' (metastable). **c**, as $\theta \to -\pi/4$ the two minima continue to approach in energy, and form a degenerate ground state at $\theta = -\pi/4$, with a Josephson phase $\pm\varphi$. All energy profiles correspond to zero bias current. The $U_j(\theta,\alpha)$ plots are adopted from Ref. [17]. **d**, phase variation across a ChDW. Two chiral domains (coloured boxes) are separated by a ChDW (the blank space in between) with an arbitrary orientation. Colours indicates the orbital phaseof the order parameter, which winds in a different direction for each domain. ChDW orientation is represented by the direction of the transport channel that connects the two domains (solid arrows). θ is defined as the angle between the ChDW plane and the normal to the transport direction (dashed line). If $\theta = 0$, the arrow connects the left and right domains via the same phase (red on both sides). As $\theta : 0 \to -\pi/4$, the orbital phase of the left domain is no longer equal to that of the right domain, giving rise to an arbitrary Josephson phase.

Sigrist *et al.* showed that, in addition to the usual phase difference between two sides of the weak link α, the Josephson energy of a ChDW would also be a function of the relative alignment of the two domains with respect to the direction of transport. This concept is illustrated in Figure 7.13, where θ represents the angle between transport direction (represented by arrows in Figure 7.13 **d**) and the normal to the plane of ChDW. When the bias current is perpendicular to the ChDW ($\theta = 0$), $U_J(\alpha, 0)$ has one stable ground state at $\alpha = 0$, and one metastable state at $\alpha = \pi$. In this case the ChDW operates as a 0-junction, meaning that — in the absence of external flux — there is zero phase difference between the left and the right side of the junction. However, as we see in Figure 7.13 **b,c**, the two states change their energies depending on the orientation of ChDW.

Figure 7.13 **b** shows the energy of a system where the transport direction makes a $\theta = -\pi/8$ angle with the normal to the ChDW plane. This raises the energy of the stable state (previously at $\alpha = 0$), and lowers the energy of the metastable state. More striking however, is that the ground state has developed an arbitrary phase of φ_0, which is neither zero or π. The offset in the phase of the ground state has profound consequences on the physics governing the junction, as it means that there would be a finite flow of supercurrent in the *absence* of external bias or magnetic flux. This anomalous current breaks the symmetry between leftward and rightward transport across the junction, which is referred to as the chiral symmetry (not to be confused with the chirality of the order parameter). In this sense, a ChDW acts as the so-called φ_0-junction, whose energy profile has a single ground state with a phase offset of φ_0. The main difference here being the presence of an additional metastable state φ'.

As $\theta \to -\pi/4$, the two states of $U_J(\alpha,\theta)$ continue to approach in energy, and ultimately form a degenerate ground state at $\theta = -\pi/4$ (see Figure 7.13 **c**). This energy profile corresponds to that of the so-called φ-junction, which has a bistable zero-voltage state with phases $\alpha = \pm\varphi$. This has been realised in junctions with parallel 0 and π segments, which have been carefully tuned to yield a spatially averaged phase that is neither 0 nor π [25, 26]. A unique characteristic of the ϕ-junction is that the $I-V$ can exhibit two critical currents. In Ref. [26] the authors show that their junction can be prepared in either one of $+\varphi$ or $-\varphi$ states. Depending on the current sweep sequence, there would be a step on one side of the $I-V$ trace, corresponding to the transition from $\pm\varphi$ phase to $\mp\varphi$. For instance, if the system is in the $+\varphi$ state, sweeping the current with a positive bias would result in a single I_c^+ as the phase escapes $+\varphi$ (i.e. in Figure 7.13 **c**, the ball in $+\varphi$ begins to roll down the right side of the "washboard potential"). Now consider what happens when we bring the applied bias back to zero, and continue to sweep the current in the negative direction. As $I^+ \to 0$, the phase gets initially re-trapped in the $+\varphi$ minimum, which it escapes as we continue sweeping $I: 0 \to I^-$ (i.e. tilting the energy profile to the left) but gets trapped again by the $-\varphi$ minimum before it enters the dynamic regime (i.e. rolling down the left side of the washboard potential). This results in two zero-voltage states: first by retrapping at $+\varphi$, and then by the energy well at $-\varphi$. The second zero-voltage state manifests itself as a step in the $I-V$, which appears on the left-hand side of the trace (negative bias). If we now reverse this sequence by sweeping the bias as $I^- \to I^+$, the

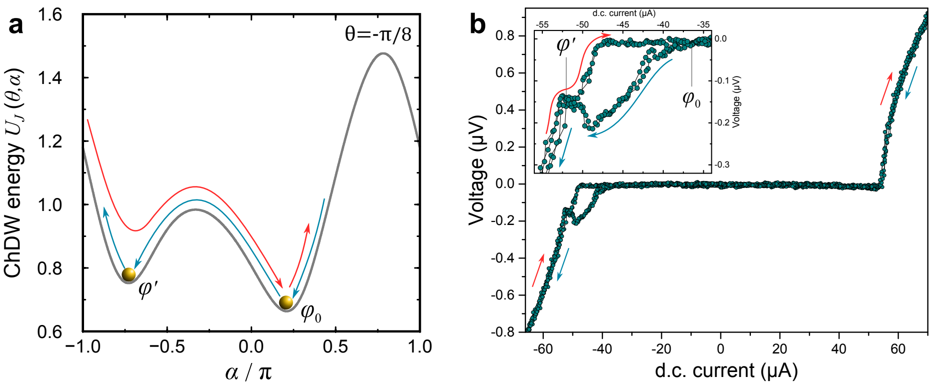

Figure 7.14: $I-V$ behaviour of a ChDW junction with an arbitrary orientation. **a**, Josephson energy of the ChDW for $\theta=-\pi/8$, in the absence of bias current $I=0$ (adopted from Ref. [17]). Red and blue arrows represent forward reverse sweeps of bias current, respectively. In the absence of bias current, the phase is trapped at φ_0. Sweeping the current as $I: 0 \to I^+$ would result in a single I_c as the phase escapes φ_0 ($V \neq 0$). In the reverse sweep $I^+ \to 0$, the phase is retrapped at φ_0. Sweeping with a negative bias current would tip the energy profile to the left. The phase leaves the φ_0 minimum, but is subsequently trapped by the local minimum at φ', where it remains before entering the dynamic regime ($V \neq 0$). As we sweep the current back to zero, the phase is momentarily retrapped by the local minimum at φ', before making its way to the global minimum at φ_0. We used $\theta=-\pi/8$ to represent the $I-V$ characteristics of the entire class of $0<|\theta|<\pi/4$. The magnitude of critical and retrapping currents would depend on the depth of the minima and the exact value of θ. However, φ_0 and φ' ensure that there will be multiple static regimes in the $I-V$ curve, and that they will not be symmetric with respect to the sign of I. **b**, $V(I)$ measured at $\mu_0 H_z = 2$ mT ($H_{ab}=0$) by scanning I as $I^+ \to I^- \to I^+$ in multiple cycles. The same convention as **a** is used to indicate the sweep direction. By reasoning that if $\Delta V/\Delta I = 0$ (static phase), the phase must be trapped by a minimum of energy (either local or global), it is easy to see how this unusual $I-V$ can arise from an energy profile similar to the one depicted in **a**.

step would appear on the right-hand side of the $I-V$ (assuming damping is not too small). A clear example of such $I-V$ behaviour can be found in Ref. [25] (Fig. 4).

In order to have multiple zero-voltage states, there needs to be multiple minima in the energy profile of the junction. For instance, the asymmetric $I-V$ characteristic of the φ-junction does not apply to φ_0 junctions, where the Josephson energy has a single minimum. This brings us back to Figure 7.13 **b**, which represents the most general configuration of a ChDW, as it includes all orientations within $0<|\theta|<\pi/4$ (as opposed to 7.13 **a,c**, which correspond to special angles $\theta=0,\pm\pi/4$). For convenience however, we continue to use the example of $\theta=-\pi/8$ in the following discussion. What makes this type of $U_J(\alpha,\theta)$ so intriguing is that it contains elements of both φ_0- and φ-junctions. It is similar to the φ_0-junction, in a sense that there is only one ground state — with an arbitrary phase offset, but it also resembles the double-well energy profile of the φ-junction – due to its metastable state at φ'. As φ_0 and φ' states are not degenerate, it raises the question how the $I-V$ behaviour would be affected by this asymmetric energy profile.

In Figure 7.14 **a** we consider the same current sweep sequence as we did when describing the φ-junction above. Initially the system is in its ground state φ_0. Applying a positive current bias (red arrow) would tilt the energy profile to the right, and produce a single I_c^+.[2] As we reverse the current back to zero (blue arrow) the phase is re-trapped at φ_0. This brings the junction back to its static regime, resulting in zero voltage. We then sweep the current with a negative bias (i.e. tilting the energy profile to the left), and the phase crosses-over from φ_0 to φ'. Once at φ', the phase remains static ($V = 0$) up to I_c^-.

So far the Josephson energy profile in Figure 7.14 **a** has produced the same $I - V$ characteristics as a φ-junction with a doubly degenerate ground state. There is a single critical current on one side of the $I - V$ (where the phase escapes φ_0), and two on the other side (one for $\varphi_0 \rightarrow \varphi'$, and another one when it leaves φ'). The distinction however becomes clear when we sweep the negative bias back to zero. In contrast to the φ-junction, the asymmetric structure of $U_J(\alpha,\theta)$ guarantees the φ_0 state to have a lower energy every time the bias is removed. Hence, depending on the energy difference between φ' and φ_0, which in turn depends on θ, the two critical currents would consistently appear one side of the $I - V$ (as opposed to the φ-junction, where they can switch to either side). For $-\pi/4 < \theta < 0$, this would be the left-hand side of the $I - V$ (negative bias), and for $0 < \theta < \pi/4$, the step would appear on the right-hand side, since $U_J(+\alpha,-\theta) = U_J(-\alpha,+\theta)$.

As Figures 7.14 **b** and 7.12 show, the $0 < |\theta| < \pi/4$ scenario provides a rather apt description of the observed $I - V$ anomalies. We now continue by examining how $\theta \neq 0$ can occur in our structure. First, we make a note that the $I - V$ anomalies only appear at low temperatures, where a single ChDW is expected to be crossing the arms of the ring, as shown in Figure 7.5 **a & c**. In this regime $T \ll T_c$, the ChDWs are small enough to have a well-defined position and orientation with respect to the ring, and each other. In contrast, for $T \approx T_c$, overlapping chiral domains cover the entire ring (Figure 7.5 **b**) with no specific alignment, which makes this picture consistent with the absence of $I - V$ anomalies at $T = 1.5$ K.

Time-dependent Ginzburg-Landau simulations show that, when subjected to a d.c. current bias, a ChDW tends to orient itself along the direction of the applied current [18]. In our experiments, the anomalies emerge from the minima of the $I_c(H_z)$ pattern (Figure 7.12), where the circulating current in the ring is at its maximum. As the circulating current is added to the measurement current in one arm, and subtracted from the other, it creates an imbalance in the currents experienced by the ChDW. At $\Phi \sim \Phi_0/2$ the difference in currents could be sufficient to have a finite impact on the orientation of the ChDW.

The applied field H_z could also be playing a role by changing the position of the ChDW in each arm, as shown in Figure 7.5 **c**. While this may not directly affect θ

---

[2] Note that the asymmetric profile in Figure 7.14 **a** corresponds to the zero bias state i.e. $U_J(\alpha,\theta = -\pi/8)$ is not “tilted” by some external bias. The role of bias currents is shown in the form of red and blue arrows, which the phase can follow.

(i.e. orientation with respect to transport direction), H_z can modify the orientation of ChDWs relative to each other. This situation is discussed in Ref. [38], which considers a ring with a pair of ChDWs radially crossing its wall. Modelling the arbitrary angle between the ChDWs as the bending of a single ChDW, the authors argue that such a system can host fractional vortices, including the half-quantum vortex (HQV) at $\Phi \approx n\,\Phi_0/2$. It is worth noting that this HQV is different from the one discussed in Chapter 6, which could exist even in the absence of ChDWs. The entire phase winding of this HQV is carried out by the orbital component of the chiral states. As there is no winding of spin phase, this type of HQV is not accompanied with a spin-polarization, which means that it can be stable even in the absence of external fields H_{ab}.

Lastly, we discuss the role of in-plane fields H_{ab} in our experiment. As shown in Figure 7.12 the $I-V$ anomalies show a direct dependence on the sign and magnitude of H_x. The anomalies grow larger with the field and, more importantly, their symmetry is determined by the direction of H_x. Figure 7.12 **c** ($\mu_0 H_{ab} = -1$ mT) shows the $I-V$ pattern can be mirrored by switching the field polarity. As described above, if a ChDW is oriented at θ, where $-\pi/4 < \theta < 0$, the step in the $I-V$ would occur for the negative current bias. This however would be reversed if the ChDW was to change its orientation as $-\theta \rightarrow \theta$, in which case the energy profile would be mirrored in the phase space i.e. $U_J(+\alpha, -\theta) = U_J(-\alpha, +\theta)$. For instance, if $\theta : -\pi/8 \rightarrow \pi/8$, the φ' phase in Figure 7.14 **a** would become the ground state, and φ_0 would be metastable.

While one could argue that the applied H_x may have modified the orientation of the ChDW, a coupling between H_{ab} and the chiral components would be rather unlikely [3]. There is however a distinct possibility for H_{ab} to couple to the spin of Cooper pairs. Spin-susceptibility experiments on $\mathrm{Sr_2RuO_4}$ have demonstrated that an external H_{ab} would introduce an imbalance between $|\uparrow\uparrow\rangle$ and $|\downarrow\downarrow\rangle$ states, which results in a finite spin polarization [39, 40] [4].

The spin polarization can play a role in our experiments in a number of ways. Here, we mention two. The first one is concerned with stabilizing half-quantum vortices (HQVs) through Zeeman coupling – as described in Chapter 6. This is consistent with the fact that the $I-V$ anomalies emerge at $\Phi \approx \Phi_0/2$, and that they grow larger with H_x, as the field should lower the energy of the HQV states. This however does not account for the observed asymmetry of the anomalies. Also, the in-plane fields used here are at least an order of magnitude smaller than the ones used in previous reports on HQV (in both Ref. [41] and Ref. [19] the signatures of HQV appear for $H_{ab} > 8$ mT).

A more reasonable explanation is that H_{ab} modifies the Josephson energy of the

---

[3] In order to change the domain configuration, a magnetic field would need to couple to the orbital angular momenta of the domains, which are expected to lie along the c-axis of $\mathrm{Sr_2RuO_4}$ lattice.

[4] Note that the spin-susceptibility measurements needed to apply H_{ab} fields that were 2 to 3 orders of magnitude larger than the fields used in our experiments.

ChDW by introducing a non-zero spin current. The energy profiles in Figure 7.13 were formulated for a system with no spins [17]. There is however no reason to assume these profiles would remain unchanged in presence of a finite magnetization. For instance, the magnetization induced by H_{ab} could potentially lower the energy of φ' relative to φ_0, and vice versa. However, there are currently no theoretical studies on the energy of a ChDW as a function of spin polarization. Such information could be rather valuable.

SUMMARY OF THE ANOMALOUS CURRENT-VOLTAGE BEHAVIOUR

To summarise, the current-voltage measurements show multiple zero-voltage states, which requires the Josephson energy profile U_J to have more than one minimum. The additional zero-voltage state, which appears as a step in the $I-V$ measurements, has a distinct asymmetry with respect to the *sign* of the bias current. Regardless of sweep direction for I, the step constantly appears on the same side of the $I-V$ (in the absence of H_{ab}). This exotic behaviour is accounted for by an asymmetric Josephson energy which has one global and one local minimum, corresponding to a stable φ_0 and a metastable φ' Josephson phase, respectively, where φ_0 and φ' can take on any values between 0 and π. While most unconventional for usual Josephson junctions, this is a strikingly apt description of the predicted ChDW energy [17], particularly if the ChDW plane is not precisely perpendicular to the transport direction. TDGL simulations of our ring, show this condition could be realised at $T \ll T_c$, where the ChDW is small enough to develop a well-defined orientation (as opposed to $T \approx T_c$, where overlapping chiral domains extend over the entire ring), as shown in Figure 7.5. This is also consistent with our measurements, where the $I-V$ anomalies appear at 0.78 K, but are absent at 1.5 K. As for the cause of ChDW misalignment, we discuss a number of possibilities, the most likely of which being the circulating currents.

The $I-V$ anomalies show a direct dependence on small in-plane fields. They grow larger with H_x amplitude, and their asymmetric form is mirrored (with respect to I) by switching the direction of H_x. We attribute this to field-induced spin-polarization of equal-spin triplet Cooper pairs. We expect this finite magnetization to modify the symmetry of the Josephson energy profile. Currently, we lack the theoretical framework that can describe transport across a spin-polarized ChDW. Regardless of this, the reversible nature of $I-V$ anomalies makes it very clear that the effect is not stochastic, and corresponds to a robust mechanism which is yet to be understood. Fortunately, with the use of order parameter simulations and controllable mesoscopic structures, there is a real possibility of this in the near future.

Lastly, we note that due to the absence of external components in our system (s-wave electrodes, Ru inclusions, 3 K-phase, etc.), the $I-V$ anomalies – and the breaking of time-reversal symmetry which they represent – could only correspond to the intrinsic order parameter of Sr_2RuO_4.

7.5. SUMMARY & OUTLOOK

The existence of a p-wave chiral order parameter in Sr_2RuO_4 would make this a rare exception to currently known superconductors. Establishing this requires irrefutable evidence of *chirality*, which is expected to reveal itself in the form of superconducting chiral domains with spontaneous edge currents. The search for chiral domains however, has proven to be a challenging endeavour. The present study implements a new approach to this by focusing on the properties of a *single* chiral domain wall (ChDW) in a mesoscopic crystal.

It has been proposed that by locally suppressing the order parameter, a ChDW would act as an unconventional Josephson junction. We investigate this by performing transport experiments on mesoscopic rings, structured entirely out of a single (and homogenous) Sr_2RuO_4 crystal. Order parameter simulations predict this system to a have multi-domain ground state, with a ChDW crossing the arms of the ring, where it forms a pair of parallel Josephson junctions.

Our transport measurements show a clear I_c oscillation, similar to that of a DC SQUID with two symmetric Josephson junctions. The oscillations emerge together with the superconducting transition, and are continuously present in all the measurements down to $T \ll T_c$. We evaluate this behaviour in the terms of conventional types of weak link (e.g. nano-bridges, phase-slip lines, proximity junctions etc.). Each case shows clear discrepancies, and fails to describe our observations. Furthermore, the SQUID oscillations are entirely absent in structures with a finite level of disorder or strain, indicated by the enhancement of $T_c \rightarrow 3$ K (i.e. the "extrinsic" phase of Sr_2RuO_4). These systems behave as standard superconducting loops, showing only T_c oscillations which appear in the form of small-amplitude magnetoresistance near T_c.

In addition to the abovementioned SQUID oscillations, we also observe anomalous current-voltage characteristics, which also represent the breaking of time reversal symmetry. More specifically, repeated current sweep measurements show two distinct critical currents that only appear on one side of the $I-V$ curve. Qualitatively, this striking behaviour can be described by the unusual energy profile of a ChDW, which is predicted to have two minima of different energies. This leads to one stable and one metastable phase for the junction, which would appear as a multistage $I-V$ when sweeping the bias current.

Together, these results make a compelling case for the presence of Chiral domains in the intrinsic state of superconducting Sr_2RuO_4. Combining order parameter simulations with mesoscopic structures also sets a milestone for the study and implementation of superconducting domains, allowing for detailed design and understanding of a system before the actual fabrication.

7.6. SUPPLEMENTARY FIGURES

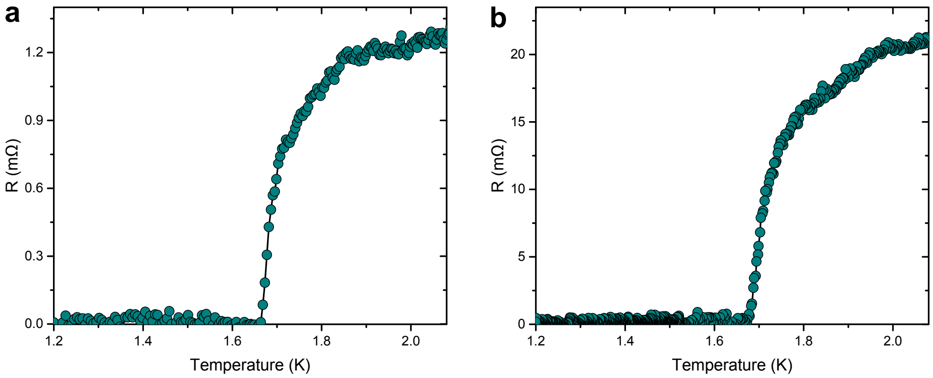

Figure 7.S1: **Superconducting transition of yy146: bulk crystal vs. structured microring**. Resistance as a function of temperature, measured before **a** and after **b** structuring with Ga$^+$ focused ion beam. The bulk crystal (**a**) and the ring (**b**) are measured using bias currents of 100 μA and 10 μA.

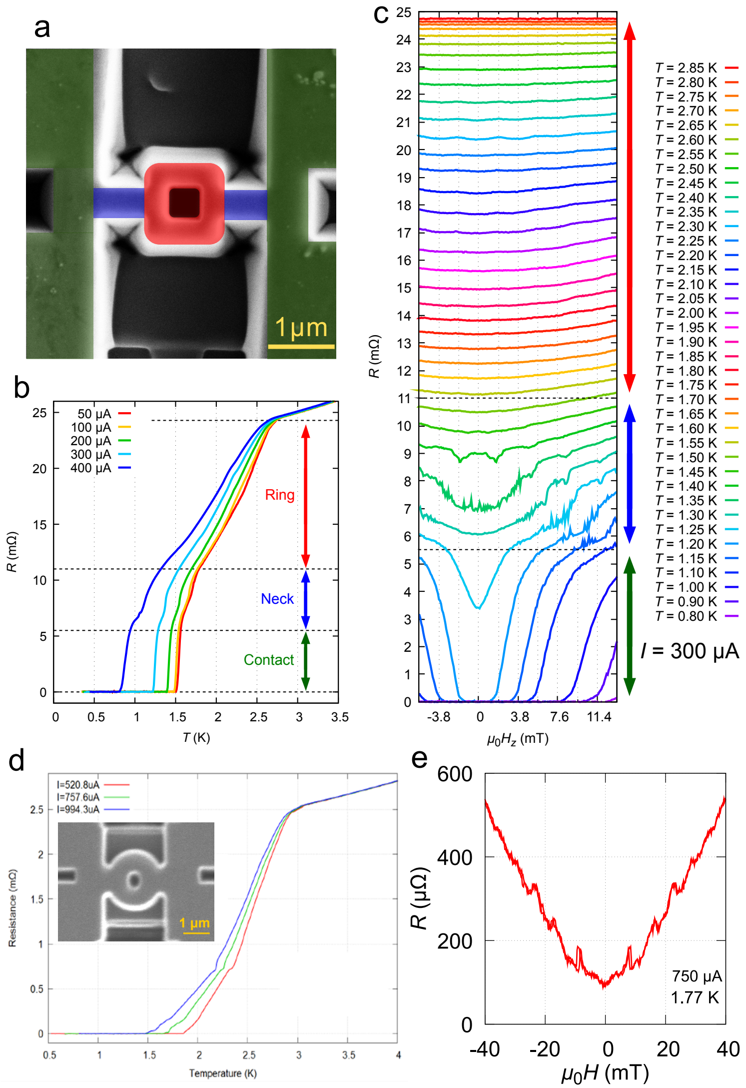

Figure 7.S2: **Rings with enhanced T_c.** Examples of rings where a finite level of disorder (i.e. stain) leads to the emergence of the “extrinsic” superconducting state in Sr_2RuO_4, characterised by the enhancement of $T_c \to 3\ K$. **a-c**, summary of transport properties of yy150 (discussed in the main text). **a**, False-colour scanning electron microscope image of the ring. This is an example of an inhomogeneous system, where the superconducting transition varies for different parts of the structure. This results in a multistage transition, which can be observed in the $R(T)$ measurements (**b**). The ring itself (red) corresponds to a broad transition with the onset at ≈ 3 K, which corresponds to the extrinsic phase of Sr_2RuO_4. In the bulk-like contacts (green), where disorder is minimal, we see a sharp transition near 1.5 K. **c**, magnetoresistance measurements at different temperatures. Little-Parks oscillations (discussed in the main text) appear in the first regime (red arrow), while the ring is still in the resistive state. SQUID oscillations are entirely absent at all temperatures. Other values of bias current (not shown here) produced the same effect. **d,e** transport measurements from yy147 (not in the main text). The crystal was not protected by the 100 nm SiO_x layer. As a result, the extrinsic phase emerges over the entire system, as indicated by the broad transition that begins at 3 K (**d**). No SQUID oscillations were found, only small amplitude magnetoresistance, driven by T_c variations (**e**).

REFERENCES

[1] A. P. Mackenzie and Y. Maeno. The superconductivity of Sr_2RuO_4 and the physics of spin-triplet pairing. *Reviews of Modern Physics*, 75(2):657, 2003.

[2] Y. Maeno, S. Kittaka, T. Nomura, S. Yonezawa, and K. Ishida. Evaluation of spin-triplet superconductivity in Sr_2RuO_4. *Journal of the Physical Society of Japan*, 81(1):011009, 2011.

[3] T. Rice and M. Sigrist. Sr_2RuO_4: an electronic analogue of ^{3}He ? *Journal of Physics: Condensed Matter*, 7(47):L643, 1995.

[4] G. M. Luke, Y. Fudamoto, K. Kojima, M. Larkin, J. Merrin, B. Nachumi, Y. Uemura, Y. Maeno, Z. Mao, Y. Mori, et al. Time-reversal symmetry-breaking superconductivity in Sr_2RuO_4. *Nature*, 394(6693):558, 1998.

[5] J. Xia, Y. Maeno, P. T. Beyersdorf, M. Fejer, and A. Kapitulnik. High resolution polar kerr effect measurements of Sr_2RuO_4: evidence for broken time-reversal symmetry in the superconducting state. *Physical Review Letters*, 97(16):167002, 2006.

[6] D. A. Ivanov. Non-Abelian statistics of half-quantum vortices in p-wave superconductors. *Physical Review Letters*, 86(2):268, 2001.

[7] S. D. Sarma, C. Nayak, and S. Tewari. Proposal to stabilize and detect half-quantum vortices in strontium ruthenate thin films: Non-Abelian braiding statistics of vortices in a $p_x + ip_y$ superconductor. *Physical Review B*, 73(22):220502, 2006.

[8] C. Nayak, S. H. Simon, A. Stern, M. Freedman, and S. D. Sarma. Non-Abelian anyons and topological quantum computation. *Reviews of Modern Physics*, 80(3):1083, 2008.

[9] A. P. Mackenzie, T. Scaffidi, C. W. Hicks, and Y. Maeno. Even odder after twenty-three years: the superconducting order parameter puzzle of Sr_2RuO_4. *npj Quantum Materials*, 2(1):40, 2017.

[10] M. Anwar, T. Nakamura, S. Yonezawa, M. Yakabe, R. Ishiguro, H. Takayanagi, and Y. Maeno. Anomalous switching in $Nb/Ru/Sr_2RuO_4$ topological junctions by chiral domain wall motion. *Scientific Reports*, 3:2480, 2013.

[11] F. Kidwingira, J. Strand, D. Van Harlingen, and Y. Maeno. Dynamical superconducting order parameter domains in Sr_2RuO_4. *Science*, 314(5803):1267–1271, 2006.

[12] Y. Maeno, T. Ando, Y. Mori, E. Ohmichi, S. Ikeda, S. NishiZaki, and S. Nakatsuji. Enhancement of superconductivity of Sr_2RuO_4 to 3 K by embedded metallic microdomains. *Physical Review Letters*, 81(17):3765, 1998.

[13] S. Kittaka, H. Yaguchi, and Y. Maeno. Large enhancement of 3-K phase superconductivity in the Sr_2RuO_4–Ru eutectic system by uniaxial pressure. *Journal of the Physical Society of Japan*, 78(10):103705, 2009.

[14] M. Anwar, R. Ishiguro, T. Nakamura, M. Yakabe, S. Yonezawa, H. Takayanagi, and Y. Maeno. Multicomponent order parameter superconductivity of Sr_2RuO_4 revealed by topological junctions. *Physical Review B*, 95(22):224509, 2017.

[15] A. Steppke, L. Zhao, M. E. Barber, T. Scaffidi, F. Jerzembeck, H. Rosner, A. S. Gibbs, Y. Maeno, S. H. Simon, A. P. Mackenzie, et al. Strong peak in T_c of Sr_2RuO_4 under uniaxial pressure. *Science*, 355(6321):eaaf9398, 2017.

[16] A. Bouhon and M. Sigrist. Influence of the domain walls on the Josephson effect in Sr_2RuO_4. *New Journal of Physics*, 12(4):043031, 2010.

[17] M. Sigrist and D. F. Agterberg. The role of domain walls on the vortex creep dynamics in unconventional superconductors. *Progress of Theoretical Physics*, 102(5):965–981, 1999.

[18] V. F. Becerra and M. Milošević. Multichiral ground states in mesoscopic p-wave superconductors. *Physical Review B*, 94(18):184517, 2016.

[19] Y. Yasui, K. Lahabi, M. S. Anwar, S. Yonezawa, T. Terashima, J. Aarts, and Y. Maeno. Half-quantum fluxoid features in the magnetotransport of Sr_2RuO_4 micro rings. *Bulletin of the American Physical Society*, 2018.

[20] Z. Mao, Y. Maenoab, and H. Fukazawa. Crystal growth of Sr_2RuO_4. *Materials Research Bulletin*, 35(11):1813–1824, 2000.

[21] X. Cai, Y. Ying, N. Staley, Y. Xin, D. Fobes, T. Liu, Z. Mao, and Y. Liu. Unconventional quantum oscillations in mesoscopic rings of spin-triplet superconductor Sr_2RuO_4. *Physical Review B*, 87(8):081104, 2013.

[22] X. Cai, Y. Ying, J. Ortmann, W.-F. Sun, Z.-Q. Mao, and Y. Liu. Magnetoresistance oscillations and the half-flux-quantum state in spin-triplet superconductor Sr_2RuO_4. *arXiv preprint arXiv:1507.00326*, 2015.

[23] W. Little and R. Parks. Observation of quantum periodicity in the transition temperature of a superconducting cylinder. *Physical Review Letters*, 9(1):9, 1962.

[24] V. Moshchalkov, L. Gielen, C. Strunk, R. Jonckheere, X. Qiu, C. Van Haesendonck, and Y. Bruynseraede. Effect of sample topology on the critical fields of mesoscopic superconductors. *Nature*, 373(6512):319, 1995.

[25] E. Goldobin, D. Koelle, R. Kleiner, and A. Buzdin. Josephson junctions with second harmonic in the current-phase relation: Properties of φ junctions. *Physical Review B*, 76(22):224523, 2007.

[26] H. Sickinger, A. Lipman, M. Weides, R. Mints, H. Kohlstedt, D. Koelle, R. Kleiner, and E. Goldobin. Experimental evidence of a φ Josephson junction. *Physical Review Letters*, 109(10):107002, 2012.

[27] S. Michotte, D. Lucot, and D. Mailly. Fluxoid quantization in the critical current of a niobium superconducting loop far below the critical temperature. *Physical Review B*, 81(10):100503, 2010.

[28] G. Berdiyorov, M. Milošević, M. Latimer, Z. Xiao, W. Kwok, and F. Peeters. Large magnetoresistance oscillations in mesoscopic superconductors due to current-excited moving vortices. *Physical Review Letters*, 109(5):057004, 2012.

[29] I. Sochnikov, A. Shaulov, Y. Yeshurun, G. Logvenov, and I. Božović. Large oscillations of the magnetoresistance in nanopatterned high-temperature superconducting films. *Nature Nanotechnology*, 5(7):516, 2010.

[30] H. Fink, V. Grünfeld, and A. López. Quantum-interference device without Josephson junctions. *Physical Review B*, 35(1):35, 1987.

[31] A. A. Golubov, M. Y. Kupriyanov, and E. Il'ichev. The current-phase relation in Josephson junctions. *Reviews of Modern Physics*, 76(2):411, 2004.

[32] A. Troeman, S. van der Ploeg, E. Il'ichev, H.-G. Meyer, A. A. Golubov, M. Y. Kupriyanov, and H. Hilgenkamp. Temperature dependence measurements of the supercurrent-phase relationship in niobium nanobridges. *Physical Review B*, 77(2):024509, 2008.

[33] A. Sivakov, A. Pokhila, A. Glukhov, S. Kuplevakhsky, and A. Omelyanchouk. Oscillations of critical superconducting current in thin doubly-connected Sn films in an external perpendicular magnetic field. *Low Temperature Physics*, 40(5):408–417, 2014.

[34] D. Hazra, L. M. Pascal, H. Courtois, and A. K. Gupta. Hysteresis in superconducting short weak links and μ-SQUIDs. *Physical Review B*, 82(18):184530, 2010.

[35] N. Kumar, T. Fournier, H. Courtois, C. Winkelmann, and A. K. Gupta. Reversibility of superconducting Nb weak links driven by the proximity effect in a quantum interference device. *Physical Review Letters*, 114(15):157003, 2015.

[36] A. Sivakov, A. Glukhov, A. Omelyanchouk, Y. Koval, P. Müller, and A. Ustinov. Josephson behavior of phase-slip lines in wide superconducting strips. *Physical Review Letters*, 91(26):267001, 2003.

[37] O. J. Sharon, A. Shaulov, J. Berger, A. Sharoni, and Y. Yeshurun. Current-induced SQUID behavior of superconducting Nb nano-rings. *Scientific Reports*, 6:28320, 2016.

[38] D. G. Ferguson and P. M. Goldbart. Penetration of nonintegral magnetic flux through a domain-wall bend in time-reversal symmetry broken superconductors. *Physical Review B*, 84(1):014523, 2011.

[39] K. Ishida, H. Mukuda, Y. Kitaoka, K. Asayama, Z. Mao, Y. Mori, and Y. Maeno. Spin-triplet superconductivity in Sr_2RuO_4 identified by ^{17}O Knight shift. *Nature*, 396(6712):658, 1998.

[40] J. Duffy, S. Hayden, Y. Maeno, Z. Mao, J. Kulda, and G. McIntyre. Polarized-neutron scattering study of the Cooper-pair moment in Sr_2RuO_4. *Physical Review Letters*, 85(25):5412, 2000.

[41] J. Jang, D. Ferguson, V. Vakaryuk, R. Budakian, S. Chung, P. Goldbart, and Y. Maeno. Observation of half-height magnetization steps in Sr_2RuO_4. *Science*, 331(6014):186–188, 2011.